Structural Basis of the Metal Specificity for Nickel Regulatory Protein NikR[†,‡]

Christine M. Phillips,[§,||] Eric R. Schreiter,[§,||,⊥] Yayi Guo,[§] Sheila C. Wang,[@] Deborah B. Zamble,[@] and Catherine L. Drennan*[,§,+]

Departments of Chemistry and Biology, Massachusetts Institute of Technology, Cambridge, Massachusetts 02139, and Department of Chemistry, University of Toronto, Toronto, ON, Canada M5S 3H6

Received October 5, 2007; Revised Manuscript Received December 7, 2007

ABSTRACT: In the presence of excess nickel, *Escherichia coli* NikR regulates cellular nickel uptake by suppressing the transcription of the *nik* operon, which encodes the nickel uptake transporter, NikABCDE. Previously published in vitro studies have shown that NikR is capable of binding a range of divalent transition metal ions in addition to Ni^{2+}, including Co^{2+}, Cu^{2+}, Zn^{2+}, and Cd^{2+}. To understand how the high-affinity nickel binding site of NikR is able to accommodate these other metal ions, and to improve our understanding of NikR's mechanism of binding to DNA, we have determined structures of the metal-binding domain (MBD) of NikR in the apo form and in complex with Cu^{2+} and Zn^{2+} ions and compared them with the previously published structures with Ni^{2+}. We observe that Cu^{2+} ions bind in a manner very similar to that of Ni^{2+}, with a square planar geometry but with longer bond lengths. Crystals grown in the presence of Zn^{2+} reveal a protein structure similar to that of apo MBD with a disordered α3 helix, but with two electron density peaks near the Ni^{2+} binding site corresponding to two Zn^{2+} ions. These structural findings along with biochemical data on NikR support a hypothesis that ordering of the α3 helix is important for repressor activation.

A number of microorganisms use nickel as an essential cofactor, including the extensively studied *Escherichia coli* and *Helicobacter pylori*. In *E. coli*, nickel is necessary under anaerobic conditions for proper functioning of hydrogenase (*1*). *H. pylori*, which colonize the acidic environment of the stomach, require the nickel-containing enzymes urease and hydrogenase to maintain a neutral pH within the cell and as an energy source, respectively (*2*, *3*). An excess of nickel ions in either organism can lead to cell death (*3*, *4*). Both organisms use transcription factor NikR to inhibit the transcription of the nickel uptake machine in the presence of surplus nickel (*5*, *6*). In *E. coli*, this metal uptake machinery is an ABC transporter (NikABCDE) (*7*), while in *H. pylori*, the monomeric metal uptake protein, NixA, is the key player (*6*). Although the apo form of NikR has no detectable affinity for DNA (*8*, *9*), stoichiometric amounts of nickel induce a binding affinity of 5×10^{-9} M for the *nik* operon in *E. coli* (*10*) and 5×10^{-8} M for the *nixA* operon in *H. pylori* (*11*). In addition to controlling the transcription of NixA (*6*), NikR regulates a number of genes in *H. pylori*, including urease accessory protein UreA (*12*) and outer membrane proteins FepA3 (*13*), FrpB4 (*2*, *13*), and ExbB (*14*).

Despite the variety of metals in the cell, most metalloproteins bind a given metal with great specificity (*15*). The origin of this specificity remains an active area of research in the bioinorganic field. For NikR, in vitro spectroscopic studies and metal binding experiments seem to contradict this basic principle, as they indicate that NikR binds a number of transition metals, including Ni^{2+}, Co^{2+}, Zn^{2+}, Cd^{2+}, and Cu^{2+} with significant affinity (*16*). While nickel is best able to stabilize NikR (*16*−*18*), a number of different transition metal ions induce substantial DNA binding affinity for NikR (*10*). To investigate how different metals bind NikR and to explore the issue of specificity, we have determined the structures of the *E. coli* NikR metal-binding domain (MBD)[1] with Zn^{2+} and Cu^{2+} bound and with no metals bound.

Structures of NikR from *E. coli* (*19*, *20*), *H. pylori* (*21*), and *Pyrococcus horikoshii* (*22*) have provided insight into the tertiary structure of the protein and the changes that occur upon nickel and DNA binding. NikR is a homotetrameric protein arranged with a central tetrameric MBD and two flanking dimeric DNA-binding ribbon−helix−helix (RHH) domains (Figure 1). A comparison between *E. coli* apo-NikR

[†] This work was sponsored by National Institutes of Health Grant GM69857 (C.L.D.), CEHS Grant P30-ES002109, the Gray Fund for Undergraduate Research (Y.G.), a Natural Sciences and Engineering Research Council Postgraduate Scholarship (S.C.W.), the Natural Sciences and Engineering Council of Canada (D.B.Z.), and the Canada Research Chairs Program (D.B.Z.).

[‡] Coordinates have been deposited in the Protein Data Bank for Zn-MBD (entry 3BKF), Cu-MBD (entry 3BKT), and apo-MBD (entry 3BKU).

* To whom correspondence should be addressed: Department of Chemistry, 16-573, Massachusetts Institute of Technology, 77 Massachusetts Ave., Cambridge, MA 02139. Phone: (617) 253-5622. Fax: (617) 258-7847. E-mail: cdrennan@mit.edu.

[§] Department of Chemistry, Massachusetts Institute of Technology.

[||] These authors contributed equally to this work.

[⊥] Current address: University of Puerto Rico, Rio Piedras, PR.

[@] University of Toronto.

[+] Department of Biology, Massachusetts Institute of Technology.

[1] Abbreviations: EXAFS, extended X-ray absorption fine structure; HEPES, 4-(2-hydroxyethyl)-1-piperazineethanesulfonic acid; GuHCl, guanidine hydrochloride; MBD, metal-binding domain of NikR, residues 49−133; NTA, nitrilotriacetic acid; PAR, 4-(2-pyridylazo)-resorcinol; RHH, ribbon−helix−helix domain of NikR, residues 1−48; rmsd, root-mean-square deviation; Tris, tris(hydroxymethyl)aminomethane; XANES, X-ray absorption near-edge spectroscopy.

10.1021/bi702006h CCC: $40.75
Published on Web 01/15/2008

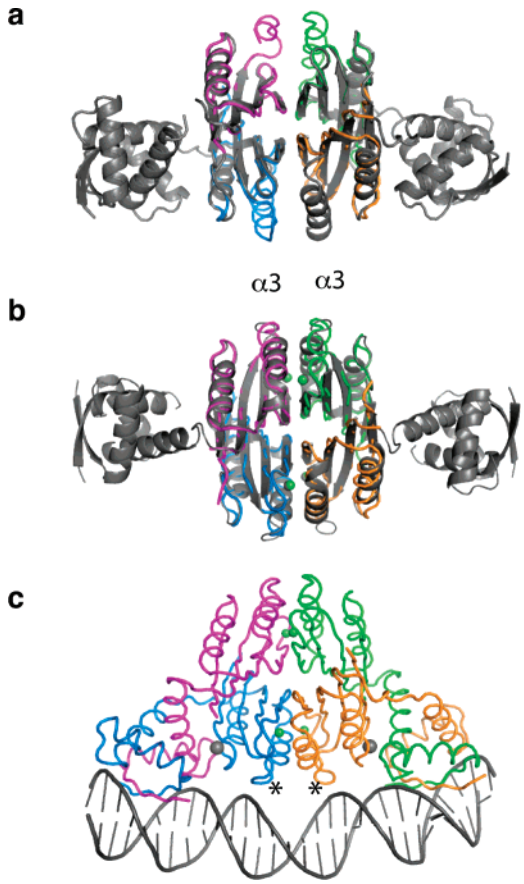

FIGURE 1: Structures of *E. coli* NikR. Each monomer composing the tetramer is a different color. (a) Alignment of apo-MBD (colored, this work) and full-length apo-NikR (gray, PDB entry 1Q5V). (b) Alignment of Ni^{2+}-bound structures of MBD (colored, PDB entry 1Q5Y) and full-length NikR (gray, PDB entry 2HZA). (c) DNA- and Ni^{2+}-bound full-length NikR (PDB entry 2HZV). K^+ ions, which were observed bound in the NikR−DNA structure, are represented as gray spheres. Asterisks denote loops and α3 helices that make connections to the DNA.

(PDB entry 1Q5V) and Ni^{2+}-bound MBD and NikR structures (PDB entries 1Q5Y and 2HZA, respectively) indicates that the α3 helices (residues 65−78) of the MBD are flexible in the absence of nickel and become structured when nickel binds to the protein (*19*, *20*). An array of structures of the Ni^{2+}−NikR complex from each of the organisms listed above (*20*−*22*) compared to the one structure of NikR bound to DNA (*20*) illustrates that the RHHs are not prearranged into the correct DNA-binding configuration upon nickel binding (Figure 1). Only in the presence of DNA are both RHHs oriented "down" in a productive DNA binding configuration. In this down DNA-binding configuration in *E. coli*, a second metal-binding site, occupied by K^+ in the crystal structure, is formed at the interface of the RHH and MBD (*20*). Binding of a cation such as K^+ to this site may serve to help lock NikR onto its DNA operator (*20*).

We have previously proposed that the MBD α3 helices play an important role in the metal-dependent response of NikR for DNA (*19*, *20*). Here we test this hypothesis by examining whether metals yielding high NikR−DNA affinity indeed stabilize the α3 helix. The structures we describe here, in combination with previously published biochemical studies, lead to a mechanism for NikR−DNA binding.

EXPERIMENTAL PROCEDURES

Determination of the Structure of Apo-MBD NikR. MBD NikR was overexpressed and purified with nickel bound as described previously (*19*). Nickel was removed from the sample by incubation with 10 mM EDTA (representing a 10-fold molar excess over MBD) at 4 °C for 48 h. The sample changed color from light yellow to colorless. To remove Ni-EDTA and excess EDTA, the sample was passed twice through Micro Bio-Spin P-6 columns (Bio-Rad).

Apo-MBD was crystallized using the hanging drop technique in a drop containing 1.5 μL of 10 mg/mL apo-MBD in buffer [20 mM Tris (pH 8.0) and 300 mM NaCl] and 1.5 μL of precipitant solution [0.2 M sodium tartrate and 20% (w/v) PEG 3350] at room temperature. Colorless, plate-shaped crystals were cryoprotected in precipitant solution containing 30% ethylene glycol.

Data were collected on beamline X12-B at the National Synchrotron Light Source (Brookhaven National Laboratory, Upton, NY) at 100 K with an oscillation step size of 0.5° per frame; data collection statistics are listed in Table 1. Reliable reflections were collected to 2.1 Å and reduced using DENZO/SCALEPACK (*23*).

The structure of apo-MBD was determined by molecular replacement with EPMR (*24*) using the protein component of the Ni^{2+}-MBD structure as a model (PDB entry 1Q5Y) (*19*). The structure was refined in CNS (*25*) with model rebuilding and adjustments made in Xfit (*26*) or Coot (*27*) to a final R_{work} of 28.8% and an R_{free} of 33.5%, with the refinement statistics listed in Table 1. Residues 66−78 of chain A and 64−79 of chain D were not observed in electron density maps and are therefore not present in the final model.

Determination of the Structure of Cu^{2+}-MBD NikR. Apo-MBD NikR was obtained as described above. Cu^{2+} was added by slow addition with vortex mixing of a 50 mM $CuCl_2$ stock solution until a $CuCl_2$:MBD stoichiometry of 1.2:1 was reached. Upon addition of $CuCl_2$, the sample became a dark yellow-orange color. Cu^{2+}-MBD was crystallized in the same form and under the same conditions as Ni^{2+}-MBD, the structure of which has been published (PDB entry 1Q5Y) (*19*). Briefly, 1.5 μL of 10 mg/mL Cu^{2+}-MBD in 300 mM NaCl and 20 mM Tris (pH 8.0) was mixed with 1.5 μL of 0.2 M disodium tartrate dehydrate and 20% (w/v) PEG 3350 in a hanging drop vapor diffusion experiment at room temperature. Deep yellow-orange crystals appeared within 2−4 days.

Crystals were cryoprotected by being briefly soaked in a precipitant solution with 20% ethylene glycol. A data set was collected on beamline 8-BM of the Advanced Photon Source (Argonne National Laboratory, Argonne, IL) at 100 K to 1.5 Å resolution (Table 1). Data were reduced using DENZO/SCALEPACK (*23*).

Crystals of Ni^{2+}-MBD and Cu^{2+}-MBD were isomorphous, so the protein component of the Ni^{2+}-MBD structure (1Q5Y) was used directly as a starting model for refinement. Refinement was carried out in Refmac 5 from the CCP4 program suite (*28*). Rigid body refinement of the MBD tetramer and individual subunits was followed by rounds of positional and *B*-factor refinement and manual refitting of the model in Xfit (*26*). After refinement of anisotropic thermal displacement parameters and addition of hydrogens in their riding positions, R_{work} = 19.5% and R_{free} = 22.7%

Table 1: Data Collection and Refinement Statistics[a]

			Zn^{2+}-MBD	
	apo-MBD	Cu^{2+}-MBD	inflection	remote
space group	*C*2	$P2_12_12_1$	$P6_222$	$P6_222$
cell dimensions				
a (Å)	67.35	45.95	46.22	46.27
b (Å)	59.67	78.44	−	−
c (Å)	75.14	81.46	124.90	125.05
β (deg)	94.01	−	−	−
wavelength (Å)	1.100	0.9791	1.2829	1.0
resolution range (Å)	50−2.1 (2.18−2.10)	50−1.5 (1.55−1.5)	40−1.9 (2.0−1.9)	28.9−1.9 (1.9−2.0)
no. of unique reflections	17408 (1685)	46684 (4006)	6755 (957)	6765 (965)
average redundancy	7.3 (2.6)	8.1 (6.1)	9.8 (6.0)	11.0 (11.4)
completeness (%)	99.5 (96.7)	97.9 (85.2)	99.5 (99.6)	99.6 (100)
$I/\sigma(I)$	17.8 (1.7)	16.9 (5.3)	28.1 (3.4)	30.6 (5.7)
R_{sym} (%)[b]	6.9 (45.1)	5.7 (25.4)	5.2 (34.5)	5.1 (35.6)
R_{cryst} (R_{free}) (%)[c]	28.8 (33.5)	19.5 (22.7)	24.9 (27.3)	
no. of protein atoms	2262	2618	509	
no. of metal ions	0	4	2	
no. of water molecules	15	171	22	
rms deviations				
bond lengths (Å)	0.008	0.011	0.005	
bond angles (deg)	1.53	1.35	1.1	
Ramachandran plot (%)				
most favored	81.3	92.2	92.9	
additionally allowed	18.7	7.8	5.4	
generously allowed	0.0	0.0	1.8	
disallowed	0.0	0.0	0.0	

[a] The numbers in parentheses are for the highest-resolution shell. [b] $R_{sym} = \sum^i_{hkl}|I^i_{(hkl)} - \langle I_{(hkl)}\rangle|/\sum_{hkl}\langle I_{(hkl)}\rangle$, where $I^i_{(hkl)}$ is the *i*th measured diffraction intensity and $\langle I_{(hkl)}\rangle$ is the mean of the intensity for the Miller index (*hkl*). [c] $R_{cryst} = \sum_{hkl}||F_o(hkl)| - |F_c(hkl)||/\sum_{hkl}|F_o(hkl)|$. $R_{free} = R_{cryst}$ for a test set of reflections (5%) not included in the refinement.

(Table 1). The final model contains residues 50−132 of NikR. One molecule of the tetramer is missing residues 64−66, which were not clearly observed in the electron density maps.

Determination of the Structure of Zn^{2+}-MBD NikR. Apo-MBD was produced as described above, and Zn^{2+} ions were added to the protein from a stock of 20 mM Zn−NTA complex to avoid MBD precipitation. The protein was allowed to equilibrate overnight at 4 °C and then was desalted by being passed through a Micro Bio-Spin P-6 column (Bio-Rad) to remove NTA. The final Zn:MBD ratio was 1:1 as confirmed spectrophotometrically with 4-(2-pyridylazo)-resorcinol (PAR) (*16*). Crystals were obtained by mixing 1.5 μL of a Zn^{2+}-MBD solution [5 mg/mL MBD in 300 mM NaCl and 20 mM Tris (pH 8.0)] with 1.5 μL of precipitant [0.1 M Bis-Tris (pH 5.5−6.5), 0.2 M $(NH_4)_2SO_4$, and 25% (w/v) PEG 3350] in a hanging drop vapor diffusion experiment at room temperature. Colorless hexagonal crystals with dimensions of 140 μm × 80 μm × 80 μm grew in 2−5 days. Three brief, consecutive soaks in solutions with increasing ethylene glycol concentrations (5, 12, and 20%) were performed to prevent the crystals from cracking during cryoprotection.

A data set was collected for the Zn^{2+}-MBD crystals at the Stanford Synchrotron Radiation Laboratory (SSRL) in Palo Alto, CA, on beam line 9-2 at 100 K at both the zinc inflection wavelength (1.2829 Å) and a remote wavelength (1.00 Å). Crystals diffracted to 1.9 Å, and data were integrated in MOSFLM (*29*) and scaled in Scala (*30*).

The protein crystallized as a tetramer as in all other NikR structures, but with one molecule of MBD per asymmetric unit (asu) instead of the typical four. The whole protein component of one MBD monomer from the Ni^{2+}-MBD structure (1Q5Y) was used as a search model for molecular replacement using PHASER (*31*). A good solution was found in $P6_222$ (*Z* score of 24) and was refined in CNS (*25*) against the inflection wavelength (1.2829 Å) data set by rigid body refinement followed by simulated annealing. The α3 helix of the MBD is mostly disordered, as in the apo-MBD and apo-NikR (1Q5V) (*19*) structures. This helix was removed from the model, and alternating cycles of positional and *B*-factor refinement with manual refitting in Coot (*27*) were carried out. The final model refined to an R_{work} of 24.9% and an R_{free} of 27.3% and includes one subunit of the MBD NikR (residues 50−61 and 80−130), 22 water molecules, and two zinc ions (Table 1).

All structures were validated using composite omit maps generated in CNS (*25*) and examined in Xfit (*26*) or Coot (*27*).

Criteria for Including α3 in the Model. NikR crystal structures sometimes show little or no electron density in the region of helix α3. In some cases, we have left some or all residues in helix α3 out of the final coordinates due to a lack of confidence about the positioning of these atoms. Our criteria for deeming α3 too disordered to model are as follows: (1) *B*-factors of ≥25 Å^2 higher for α3 residues than for the rest of the structure, (2) 50% or more of the C_α atoms not in $2F_o - F_c$ density following a few rounds of refinement, (3) more negative $F_o - F_c$ density around this portion of the structure than is typical, and (4) composite omit map density missing for more than 50% of the helical atoms.

Circular Dichroism of Ni^{2+}, Cu^{2+}, Zn^{2+}, and Apo-MBD. The MBD of NikR was expressed and purified on a Ni^{2+}-NTA column (Qiagen, Valencia, CA), followed by incubation with EDTA and anion exchange chromatography, as previously described (*8*, *16*). An assay with Ellman's reagent

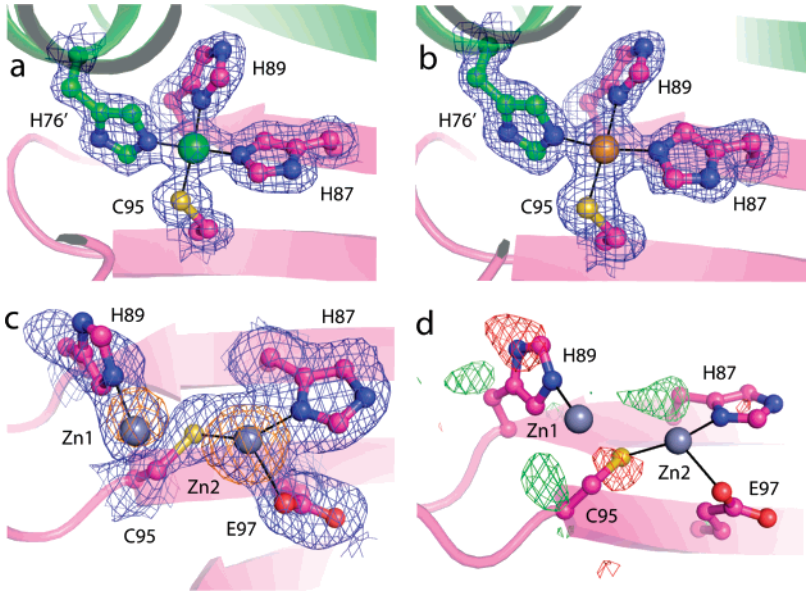

FIGURE 2: Metal binding sites with $2F_o - F_c$ electron density (blue) contoured at 1σ around metal and ligands. One monomer is colored magenta and the other green: (a) Ni^{2+}-MBD, (b) Cu^{2+}-MBD, and (c) Zn^{2+}-MBD. The dispersive difference map (orange) was calculated by subtracting data collected at 1.2829 Å (zinc inflection wavelength) from 1.00 Å (a remote wavelength) and indicates the presence of zinc, contoured at -8.0σ. (d) Zn^{2+}-MBD with $F_o - F_c$ difference density maps around the zinc binding sites with positive difference electron density colored green contoured at 3σ and negative difference electron density colored red contoured at -3σ.

and β-mercaptoethanol as a standard was used to confirm that the MBD was fully reduced, and a HPLC assay was used to confirm that the protein was in the apo form (*32*). Circular dichroism spectra were collected on a Jasco model J-710 spectropolarimeter in a cylindrical cell with an optical path length of 0.1 cm over a wavelength range of 260−195 nm at room temperature, as previously described (*16*). Each CD spectrum was the average of five accumulations at a scanning speed of 50 nm/min, a 1.0 nm spectral bandwidth, a data pitch of 0.1 nm, and a 4 s response time. The experiments were performed by using protein stocks dialyzed against 10 mM HEPES and 100 mM KCl (pH 7.6) at concentrations ranging from 5 to 40 μM. For experiments performed in the presence of metal, the protein was first incubated overnight with stoichiometric amounts of metal sulfate at room temperature. The concentrations of the holoprotein stocks were verified by diluting the protein in 6 M GuHCl and EDTA and measuring the absorbance at 280 nm, using the calculated extinction coefficient of 2680 M^{-1} cm^{-1} (*33*). Following data collection, the absorbance at 220 nm was analyzed to determine the percent helicity of each structure using eq 1

$$\% \ \alpha \text{ helix} = [(-\theta_{222} + 3000)/39000] \times 100 \qquad (1)$$

where θ_{222} is the mean residue ellipticity at 222 nm (*34*−*36*).

RESULTS

Full-Length versus MBD NikR Structures. The isolated MBD of NikR is a simple model system that can be used to study the structural consequences of binding of a transition metal ion to the protein. The MBD of NikR (residues 48−133) contains the residues involved in high-affinity metal binding but lacks the N-terminal ribbon−helix−helix (RHH) DNA-binding domains. This domain retains all key metal binding features of the full-length NikR while crystallizing much more readily. The isolated MBD is tetrameric and has a topology identical to that of the MBD portion of the full-length NikR protein (Figure 1). The rmsd for structural alignment of Ni^{2+}-MBD (PDB entry 1Q5Y) (*19*) and full-length Ni^{2+}-NikR (PDB entry 2HZA) (*20*) is 0.89 Å for 321 C_α atoms and 1.13 Å for all 2387 common atoms. Similarly, the apo-MBD aligns with the previously described apo-NikR (PDB entry 1Q5V) (*19*) with a rmsd of 0.67 Å for 261 C_α atoms and 0.96 Å for all 1910 common atoms. All structural alignments and rmsd calculations were conducted in LSQMAN (*37*).

Metal-Binding Sites. The previously determined crystal structure of Ni^{2+}-MBD (PDB entry 1Q5Y) (*19*) shows that nickel binds in a square planar geometry at the interface between two subunits of the NikR tetramer and is coordinated by H87, H89, and C95 of one monomer and H76 of a neighboring monomer (Figure 2a). The Cu^{2+}-MBD structure described here illustrates that copper binds with the same square planar geometry and ligands as nickel (Figure 2b), with slightly longer metal−ligand distances than in the Ni^{2+}-MBD structure (Table 2). The two distances that are lengthened the most are from residues directly opposite each other (H89 and C95), creating a slightly asymmetric square planar site.

The protein used for crystallization contained one Zn^{2+} ion per MBD monomer, yet two zinc binding sites were detected in each monomer through dispersive difference electron density maps (Figure 2c). After refinement of the protein structure, the occupancies of the zinc sites were refined in CNS (*25*) while the *B*-factors of the zinc ions were restrained to values similar to those of the surrounding ligands. This refinement provided occupancies for the two zinc sites of 25 and 57%. It should be noted that the refinement of occupancies in this manner is not quantitative as we had to estimate the *B*-factors of the metals ions on the basis of those of surrounding residues and were not able to refine *B*-factors with occupancies simultaneously at this

Table 2: Distances and Angles around the Metals in the Metal-Bound MBD Structures[a]

	Ni-MBD	Cu-MBD	Zn1	Zn2
M−H76′ (Å)	1.85(7)	2.00(5)		
M−H87 (Å)	1.94(5)	2.09(6)		1.99
M−H89 (Å)	2.01(4)	2.40(2)	2.21	
M−C95 (Å)	2.22(3)	2.43(3)		2.32
M−E97 (Å)				2.34
H76′−M−C95 (deg)	88(2)	94(4)		
H76′−M−H87 (deg)	175(2)	164(7)		
H76′−M−H89 (deg)	88(2)	76(16)		
C95−M−H87 (deg)	93(1)	99(3)		131
C95−M−H89 (deg)	175(2)	170(3)		
H87−M−H89 (deg)	91(1)	84(5)		
H87−M−E97 (deg)				90
C95−M−E97 (deg)				120

[a] Distances and angles were averaged over the four monomers of the Ni^{2+}- and Cu^{2+}-bound structures. The numbers in parentheses refer to the last digits of the mean and represent the standard deviation of the measurement.

resolution. While the relative occupancy values are meaningful, the total occupancy is less so.

Zinc binding sites are located in the same region of the MBD as the copper and nickel sites and use three of the same ligands (Figure 2c). Approximately 25% of the monomers in the crystal have Zn in zinc site Zn1, located near H89 (Figure S2a of the Supporting Information). Closer to 57% of the monomers in the crystal have Zn coordinated by residues C95, E97, and H87 in zinc site Zn2 (Figure S2b of the Supporting Information). Both Zn1 and Zn2 are poor zinc binding sites with only one ligand and three ligands in our structure ordered for coordination, respectively. Zinc ions prefer a tetrahedral environment (*38*), and neither site has four ligands or angles befitting a tetrahedral geometry (Table 2). Water molecules (or another small ligand), which should be visible at 1.9 Å resolution, are not indicated by the presence of positive $F_o - F_c$ density near either zinc ion. In addition, H76 from α3, which ligates both nickel and copper from a neighboring MBD monomer, is disordered and cannot be modeled in the zinc structure. Even the residues that can be modeled at these sites are not well ordered as indicated by the presence of both positive and negative $F_o - F_c$ difference electron density around these residues (Figure 2d). Since the electron density observed is an average of all molecules in the crystal, it is likely that residues H87, H89, and C95 adopt different conformations in molecules that have Zn in site Zn1 than in molecules that have Zn in site Zn2, as indicated by the positive and negative difference electron density shown in Figure 2d. The dominant conformation of the residues is the one that provides better coordination of Zn2 as shown in Figure 2c and Figure S2b of the Supporting Information. The minor conformation in the crystal, where zinc is bound at Zn1, is shown in Figure S2a of the Supporting Information.

The nickel (*19*) and copper structures maintain two hydrogen bonding networks that each connect two of the four metal binding sites in the tetrameric MBD. This network stretches across the MBD interface and includes two residues from the α3 helix, but the network is not ordered in the apo-NikR (*19*) or apo-MBD structures. Thus, this network could be involved in stabilizing both helix α3 and the overall structure of NikR for DNA binding. In contrast to Ni^{2+}- and Cu^{2+}-MBD structures, this hydrogen bonding network is greatly disturbed in the Zn^{2+}-MBD structure (Figure 3).

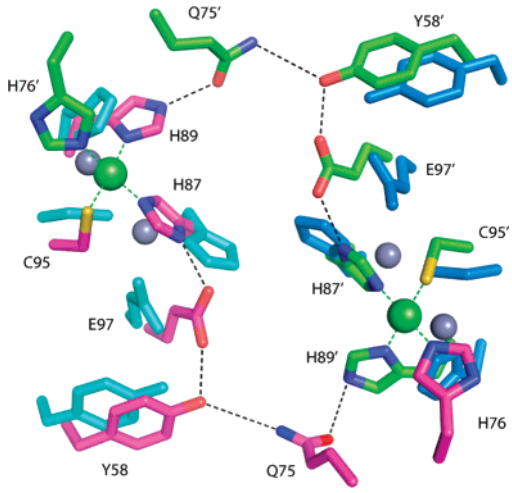

FIGURE 3: Hydrogen bonding network connecting two nickel binding sites. Zn^{2+}-MBD (colored cyan and blue) aligned with the Ni^{2+}-MBD structure with carbon atoms colored green and magenta, oxygens red, sulfurs yellow, and nitrogens blue.

Helix α3. Helix α3, residues 65−78 (Figure 1b,c), has been implicated in the mechanism of binding of NikR to DNA, due to the fact that nickel binding orders this helix and there are contacts made by residues of this helix and the preceding loop to DNA (Figure 1c) (*20*). Therefore, it is important to consider each metal's ability to order the α3 helix. The Ni^{2+}-MBD and Cu^{2+}-MBD structures have fully ordered α3 helices (Figure 4a,b and Figure S1 of the Supporting Information), with *B*-factors of the amino acids very similar to those in the rest of the structure (Table 3). The alignment of Ni^{2+}-MBD with Cu^{2+}-MBD indicates no significant change in the overall structure, with a rmsd of only 0.47 Å for all 2469 atoms in the copper and nickel structures.

The α3 helix in the Zn^{2+}-MBD structure, however, is disordered and untraceable in the electron density map (Figure 4c and Figure S1 of the Supporting Information). When helix α3 is modeled into the Zn^{2+}-MBD structure, there are large regions of the helix in negative $F_o - F_c$ difference electron density, insufficient $2F_o - F_c$ density, and higher atomic *B*-factors than in the rest of the protein (Table 3 and Figure S1 of the Supporting Information). Therefore, residues 62−78 were omitted from the Zn^{2+}-MBD structure. The rmsd for 66 C_α atoms in the Zn^{2+}-MBD and Ni^{2+}-MBD monomers is 1.24 Å, and it is 1.98 Å for all 491 identical atoms, much higher than that for Cu^{2+}-MBD compared to Ni^{2+}-MBD.

Similar to the full-length apo-NikR structure, the apo-MBD structure (Figure 4d) has poorly ordered α3 helices (Figure S1 of the Supporting Information). When modeled into the structure, the helices do not refine well in two of the four monomers, have insufficient $2F_o - F_c$ density and high *B*-factors, and are therefore either modeled as incomplete helices (monomer A) or entirely omitted (monomer D). In no case is there sufficient density to model the side chains of any α3 helix residue longer than alanine or serine. When the apo-MBD structure is aligned with the Ni^{2+}-MBD structure, the rmsd for 305 C_α atoms is 1.40 Å.

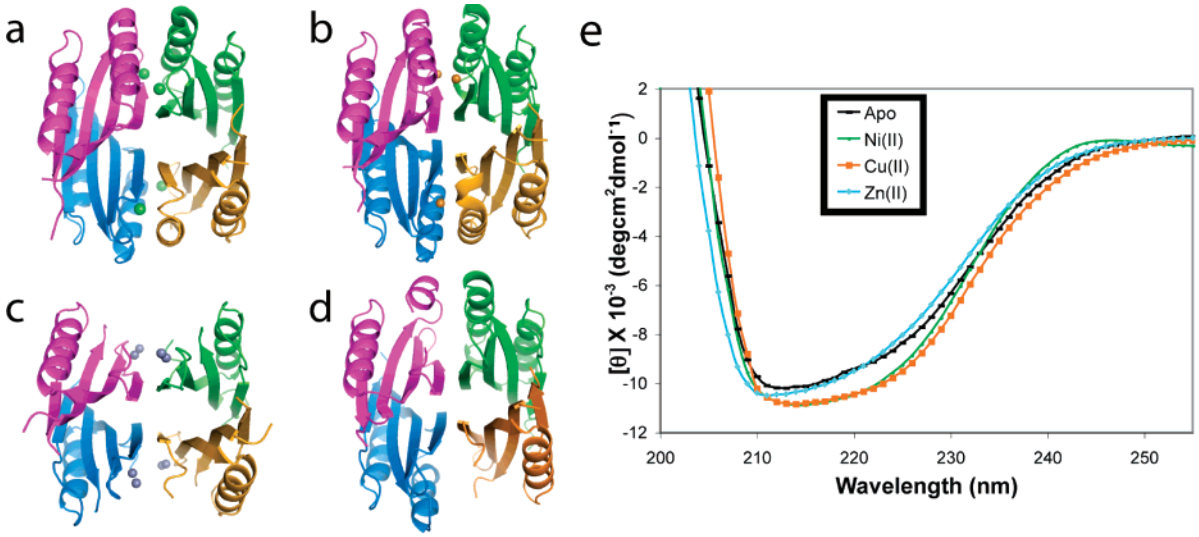

FIGURE 4: Ordering of the α3 helix. Ribbon diagrams of (a) Ni^{2+}-MBD, (b) Cu^{2+}-MBD, (c) Zn^{2+}-MBD, and (d) apo-MBD, with each monomer represented in a separate color. (e) Circular dichroism spectra of apo-, Ni^{2+}-, Cu^{2+}-, and Zn^{2+}-MBD.

Table 3: Average *B*-Factors (in square angstroms) for Different Portions of the Apo and Zn^{2+}-, Cu^{2+}-, and Ni^{2+}-Bound MBD Structures

	apo-MBD	Zn^{2+}-MBD	Cu^{2+}-MBD	Ni^{2+}-MBD (*19*)
overall structure	62.2	45.1	21.0	28.0
protein	62.3	44.6	20.6	26.8
α3 helix[a] (residues 65−78)	87.7	97.8	25.2	32.7
metals	−	47.6	23.9	19.1
metal ligands	−	42.2	18.9	22.0
water	51.7	60.7	27.1	39.3

[a] The *B*-factor for the Zn structure is an average following a single round of refinement when the α3 helix was modeled into the structure.

Circular dichroism was used to confirm differences in the α helical character of the MBD between the apo and metal-bound forms in solution. The Ni^{2+}- and Cu^{2+}-MBD structures have comparable amounts of α helicity, while the apo- and Zn^{2+}-MBD structures have less α helicity as indicated by the ellipticity at 222 nm (Figure 4e). Using eq 1, Ni^{2+}- and Cu^{2+}-MBD have approximately 9% more α helicity than the apo-MBD and Zn^{2+}-MBD forms. A fully formed α3 helix would represent ~50% of the helicity for the MBD. Thus, a decrease of 9% helicity suggests that in solution some but not all of the α3 is disordered in apo- and Zn^{2+}-MBD. This result is consistent with the broken electron density and high *B*-factors for α3 residues in these structures.

DISCUSSION

NikR's nickel-specific response in binding the *nik* operon suggests that the protein would be similarly specific in binding nickel over other metals. However, studies have shown that a number of metals are able to bind NikR, some with affinities similar to those of nickel (*16*). The measured binding affinities using competition assays for copper, nickel, and zinc with full-length NikR are 1×10^{-17}, 9×10^{-13}, and $<1 \times 10^{-12}$ M, respectively (*16*). These comparable affinities raise the question of how NikR specifically responds to nickel within the cell. The data presented here allow us to discuss how a metal's ability to order the α3 helix corresponds to its ability to increase NikR's affinity for DNA.

Metal Binding to NikR. EXAFS and XANES studies by the Maroney laboratory have indicated that Ni^{2+} and Cu^{2+} ions bind to NikR in square planar environments (*18*). The known Ni^{2+}-MBD and full-length Ni^{2+}−NikR structures are consistent with this geometry, and now we show that Cu^{2+} also binds in the same site as Ni^{2+} with the same ligands and a nearly identical coordination environment (Figure 2). Cu^{2+}-MBD has metal−ligand bond distances slightly longer than the distances in the Ni^{2+}-MBD structure (Table 2), also consistent with the trend observed through the EXAFS studies where the metal−N_{imd} distances were measured as 1.905 and 1.928 Å and metal−S distances as 2.130 and 2.210 Å for nickel and copper, respectively (*18*). The absolute values measured from the crystallographic data tend to be longer (2.22 Å for Ni−S, 2.43 Å for Cu−S, 1.93 Å for Ni−N_{imd}, and 2.16 Å for Cu−N_{imd}).

The Zn^{2+} sites observed in our structure are partially occupied, and the ligands to the metals are highly flexible. The zinc XANES data have been modeled in terms of a single Zn^{2+} ion bound to NikR with four coordinating ligands, interpreted as a tetrahedral coordination environment (*18*), which is common for divalent zinc ions. We do not observe a tetrahedral site, nor can we imagine a ligand rearrangement that would allow for a tetrahedral geometry (see angles in Table 2 and Figure 2c). Reported distances from EXAFS are 2.229 Å for the Zn−S bond and 1.990 Å for the Zn−N_{imd} bonds (*18*). Crystallographic metal−ligand distances are similar but again somewhat longer (we find values of 2.32 Å for Zn−S and 2.18 Å for Zn−N/O on average). We also observe four unique ligands to the zinc ions, three of which are N/O donors and one that is a S-donor, again consistent with the EXAFS data (*18*). Reevaluation of the Zn^{2+} EXAFS data using our model would determine if the zinc data can be fit as well to a partially occupied dinuclear zinc model as they can to a single tetrahedral zinc site.

Ordering of the α3 Helix Is Metal-Dependent. The initial structures of *E. coli* NikR provided insight into the structural changes nickel induces upon binding to the apoprotein (*19*,

Table 4: Root-Mean-Square Deviations (in angstroms) between the C_α Atoms in Apo and Metal-Bound MBD NikR Structures[a]

	apo-MBD	Zn^{2+}-MBD	Ni^{2+}-MBD	Cu^{2+}-MBD
apo-MBD	−	1.18 (65)	1.40 (305)	1.43 (305)
Zn^{2+}-MBD	1.18 (65)	−	1.24 (66)	1.20 (66)
Ni^{2+}-MBD	1.40 (305)	1.24 (66)	−	0.22 (321)
Cu^{2+}-MBD	1.43 (305)	1.20 (66)	0.22 (321)	−

[a] The number of aligned atoms is in parentheses.

20). In apo-NikR, three of the four α3 helices are disordered and not traceable in the electron density maps (residues 62−77). The Ni^{2+}-bound MBD and full-length NikR structures have complete electron density for all α3 helices with *B*-factors similar to those of the rest of the protein (Table 3). Divalent nickel and copper bind tightly to NikR and both are able to order the α3 helix, while divalent zinc binds less tightly and is incapable of ordering the α3 helix (Figure 4 and Figure S1 of the Supporting Information). Circular dichroism experiments (Figure 4e) also indicate that the Zn^{2+}- and apo-MBD complexes contain less α helicity than the Cu^{2+}- and Ni^{2+}-MBD complexes. In addition, examination of the rmsds between different structures indicates that apo- and Zn^{2+}-MBD are similar to each other, while the Ni^{2+}- and Cu^{2+}-MBD structures are structurally homologous (Table 4).

Our results are consistent with previous experiments that investigated the stability of the protein in the presence of different metals. In proteolysis experiments, nickel, and copper to a lesser extent, are able to stabilize residues 66−133, which include the α3 helix, protecting them from proteolysis, while zinc offers no (or little) protection (*17*). Chemical and thermal stability assays indicate that nickel-bound NikR requires a larger amount of guanidine HCl or a higher temperature to be denatured in comparison to any other metal-bound NikR, though copper did stabilize the protein more than zinc (*16*). Hydrogen−deuterium exchange experiments indicate that when nickel or copper is bound to the protein the exchange rate is much slower than when zinc or no metal is bound, which the authors relate to the ordering of the α3 helix (*18*).

An obvious difference between the Zn^{2+}/apo and Cu^{2+}/Ni^{2+} structures is the disorder of H76, a residue in α3, in the former and the involvement of this residue in metal ligation in the latter. In Cu^{2+}- and Ni^{2+}-bound MBD, H76 bridges the tetrameric interface by becoming the fourth ligand of the square planar metal site. It is our proposal that nickel and copper's ability to ligate this residue and in turn "tie down" the α3 helix and its preceding loop is related to the ability of Ni^{2+}- and Cu^{2+}-bound NikR's ability to bind DNA. The hydrogen bonding network across the tetrameric interface in the MBD formed only in the presence of Ni^{2+} and Cu^{2+} may also be responsible for inducing some ordering of the α3 helix (Figure 4). The disruption of this hydrogen bonding network in the apo or Zn^{2+}-bound form of NikR could play a role in determining the overall flexibility of the α3 helix observed crystallographically and by circular dichroism.

Ordering of the α3 Helix Is Linked to DNA Binding. Ordering of the α3 helix and the loop preceding it (loop 64−65) has previously been implicated in the mechanism of binding of NikR to DNA (*19*, *20*). The Ni^{2+}−NikR−DNA structure illustrates an interaction between the MBD and backbone phosphates on the DNA (marked with asterisks in Figure 1c). Some of the residues of the MBD that make these contacts are in loop 64−65, which, along with the α3 helix, is disordered in the absence of Ni^{2+}. The structures of apo-, Zn^{2+}-, and Cu^{2+}-MBD in combination with previously determined structures and DNA binding data provide further evidence that the ordering of the α3 helix is an important step in NikR's recognition of DNA.

In vitro DNA footprinting and mobility shift assays indicate that although Cu^{2+}, Ni^{2+}, Zn^{2+}, Co^{2+}, and Cd^{2+} are capable of inducing some DNA binding, Cu^{2+} and Ni^{2+} are the most efficient (*10*). Cu^{2+}- and Ni^{2+}-bound NikR have nanomolar affinity for the *nik* operon, while Zn^{2+}-NikR has a binding affinity 2 orders of magnitude lower for the operon (*10*). In vivo, LacZ reporter assays indicate that only nickel and not Mn, Fe, Co, Cu, or Zn is capable of repressing transcription of the *nik* operon (*18*). While the inability of copper to repress transcription in vivo is seemingly inconsistent with the DNA binding (*10*) and structural data, these latter results are for Cu^{2+}, not Cu^{+}, which is the form of copper that would be most abundant in the cell (*39*, *40*). While the specificity of a nickel-regulatory protein for nickel makes logical sense, if there is no free Cu^{2+} in the cell there would be no evolutionary pressure for NikR to have evolved such that Cu^{2+} would not activate it (*39*, *40*).

Mechanism of Binding of NikR to DNA. The data presented here along with previous studies suggest that there are at least three factors that are likely important in the formation of a stable complex between NikR and the *nik* operator DNA with stoichiometric nickel present: (1) hydrogen bonding and electrostatic interactions formed between MBD and DNA upon α3 ordering, (2) the proper orientation of the RHHs down such that residues of this domain can make specific contacts with DNA, and (3) the binding of K^{+}, or a similar cellular abundant cation, to a site between the RHHs and MBD, stabilizing the RHH in a down, cis DNA binding orientation. It should be noted that one turn of helix α2 of the RHH must unwind for the down RHH conformation to be obtained (*20*, *22*). It has been reported that with excess nickel NikR binds DNA with greater affinity (*8*, *10*). Whether this greater affinity is due to a specific low-affinity nickel site in NikR or to a general electrostatic effect is unknown. It is also not known if this "low-affinity" nickel effect is physiologically relevant. For the sake of simplicity, here we will consider only the mechanistic situation for NikR with stoichiometric nickel and with a second metal cation like K^{+}.

Figure 5 shows many possible DNA binding pathways, but the process most likely to occur in the cell on a regular basis consists of steps **I**−**V**. Ni^{2+} binds to the high-affinity site of NikR, stabilizing the α3 helix and its preceding loop (**I** → **II**). The NikR molecule makes initial contacts to DNA, stabilized via hydrogen bonds and electrostatic interactions between residues in the loop of the MBD and the phosphate backbone (**II** → **III**). The conformationally flexible DNA-binding RHHs are then capable of finding their binding sites in the major grooves of the DNA, enforcing contacts between the NikR molecule and DNA (**III** → **IV**). Finally, an abundant intracellular metal ion such as potassium binds at the interface of the MBD and RHHs, serving to stabilize this NikR configuration (**IV** → **V**).

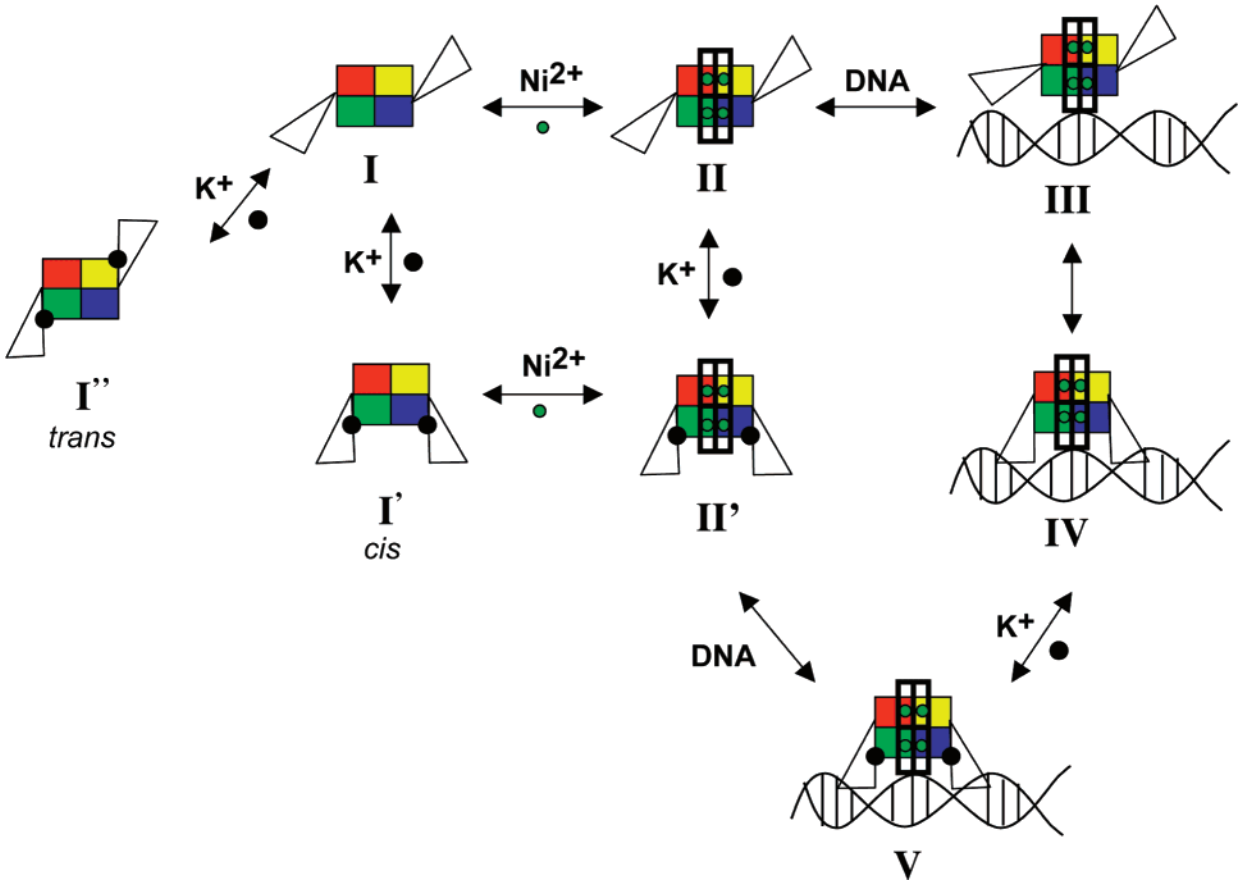

FIGURE 5: Proposed NikR regulatory mechanism. Dimeric RHHs are represented by white triangles. Each monomer of the MBD is represented in a different color. Bold empty rectangles represent ordered α3 helices. Nickel ions are represented by green circles outlined in black. Potassium ions are represented by large black circles.

While there is no experimental evidence to indicate when a cation like K^+ might bind to the RHH−MBD interface, the affinity of NikR for a cation like K^+ should be greater in the NikR−DNA complex where the RHHs are stably positioned near the MBD (Figure 5, **IV**). In the absence of DNA, RHHs are highly mobile and K^+ binding sites exist only transiently when the RHHs sample cis (**I′**) or trans (**I″**) conformations. Thus, while K^+ may bind weakly to multiple forms of NikR (**I′**, **I″**, and **II′** in Figure 5), the high occupancy of K^+ is likely only in the NikR−DNA state (**V**). Again, it is not known if the RHH or MBD binds DNA first, but we find it easiest to think about the MBD making the first contacts. The interactions between residues in the MBD with backbone phosphates in the DNA are not specific but could initially localize NikR to DNA while the protein searches for the ideal binding site. With NikR localized on DNA, the floppy RHHs will occasionally sample a down conformation, and when they do, they will make specific contacts to DNA when the correct operator sequence is available. The fact that apo-NikR does not bind DNA with measurable affinity suggests that if the RHHs bind first, they would have weak affinity until a metal-ordered MBD is also stably bound to DNA.

Conclusions. To control nickel concentrations in the cell, Nature developed a transcription factor both flexible enough to bind two half-sites separated by two turns of DNA and conformationally regulated by the binding of nickel. Interestingly, the only conformational change observed upon Ni^{2+} binding is the ordering of α3 and its preceding loop (*20*−*22*); the RHHs remain flexible (*20*−*22*). To prevent untimely repression of the *nik* operon, it is important that NikR be highly responsive to nickel ions, but not be activated by other intracellular transition metals. Divalent copper is the only metal known to induce DNA binding affinities in vitro equivalent to that of nickel. Current research suggests that any free copper in the cell is reduced to Cu^+ (*39*, *40*), which would negate any evolutionary pressure for NikR to be able to distinguish between Ni^{2+} and Cu^{2+}. Unlike Cu^{2+}, there is a significant amount of Zn^{2+} within the cell, although the amount of free zinc may be small. While Zn^{2+} can bind NikR with some affinity, it does not induce the ordering of the α3 helix, and Zn^{2+}-NikR's affinity for DNA is decreased compared to that of Ni^{2+}-NikR. Here we illustrate a correlation between the ability of a metal to order the α3 helix and that metal's ability to induce DNA binding and use this information along with previous results to describe a mechanism for binding of NikR to DNA.

ACKNOWLEDGMENT

Portions of this research were carried out at the Stanford Synchrotron Radiation Laboratory (SSRL), a national user facility operated by Stanford University on behalf of the U.S. Department of Energy, Office of Basic Energy Sciences. The SSRL Structural Molecular Biology Program is supported by the Department of Energy, Office of Biological and Environmental Research, and by the National Institutes of Health, National Center for Research Resources, Biomedical Technology Program, and the National Institute of General Medical Sciences. Use of the Advanced Photon Source (Contract DE-AC02-06CH11357) and the National Synchro-

tron Light Source at Brookhaven National Laboratory (Contract DE-AC02-98CH10886) was supported by the U.S. Department of Energy, Office of Science, and Office of Basic Energy Sciences.

SUPPORTING INFORMATION AVAILABLE

The $2F_o - F_c$ electron density around the area of the α3 helix (Figure S1) and two monomer "states" in the Zn-MBD crystal (Figure S2). This material is available free of charge via the Internet at http://pubs.acs.org.

REFERENCES

1. Unden, G., and Bongaerts, J. (1997) Alternative respiratory pathways of *Escherichia coli*: Energetics and transcriptional regulation in response to electron acceptors, *Biochim. Biophys. Acta 1320*, 217−234.
2. Davis, G. S., Flannery, E. L., and Mobley, H. L. T. (2006) *Helicobacter pylori* HP1512 is a nickel-responsive NikR-regulated outer membrane protein, *Infect. Immun. 74*, 6811−6820.
3. Mulrooney, S. B., and Hausinger, R. P. (2003) Nickel uptake and utilization by microorganisms, *FEMS Microbiol. Rev. 27*, 239−261.
4. Wu, L. F., Navarro, C., de Pina, K., Quenard, M., and Mandrand, M. A. (1994) Antagonistic Effect of Nickel on the Fermentative Growth of *Escherichia coli* K-12 and Comparison of Nickel and Cobalt Toxicity on the Aerobic and Anaerobic Growth, *Environ. Health 102*, 297−300.
5. de Pina, K., Desjardin, V., Mandrand-Berthelot, M.-A., Giordano, G., and Wu, L. F. (1999) Isolation and Characterization of the *nikR* Gene Encoding a Nickel-Responsive Regulator in *Escherichia coli*, *J. Bacteriol. 181*, 670−674.
6. Wolfram, L., Haas, E., and Bauerfeind, P. (2006) Nickel Represses the Synthesis of the Nickel Permease NixA of *Helicobacter pylori*, *J. Bacteriol. 188*, 1245−1250.
7. Navarro, C., Wu, L. F., and Mandrand-Berthelot, M.-A. (1993) The nik operon of *Escherichia coli* encodes a periplasmic binding-protein-dependent transport system for nickel, *Mol. Microbiol. 9*, 1181−1191.
8. Chivers, P. T., and Sauer, R. T. (2000) Regulation of high affinity nickel uptake in bacteria. Ni^{2+}-dependent interaction of NikR with wild-type and mutant operator sites, *J. Biol. Chem. 275*, 19735−19741.
9. Chivers, P. T., and Sauer, R. T. (2002) NikR Repressor: High-Affinity Nickel Binding to the C-Terminal Domain Regulates Binding to Operator DNA, *Chem. Biol. 9*, 1141−1148.
10. Bloom, S. L., and Zamble, D. B. (2004) Metal-Selective DNA-Binding Response of *Escherichia coli* NikR, *Biochemistry 43*, 10029−10038.
11. Benanti, E. L., and Chivers, P. T. (2007) The N-terminal Arm of the *Helicobacter pylori* Ni^{2+}-dependent Transcription Factor NikR Is Required for Specific DNA Binding, *J. Biol. Chem. 282*, 20365−20375.
12. Ernst, F. D., Kuipers, E. J., Heijens, A., Sarwari, R., Stoof, J., Penn, C. W., Kusters, J. G., and van Vliet, A. H. M. (2005) The Nickel-Responsive Regulator NikR controls Activation and Repression of Gene Transcription in *Helicobacter pylori*, *Infect. Immun. 73*, 7252−7258.
13. Ernst, F. D., Stoof, J., Horrevoets, W. M., Kuipers, E. J., Kusters, J. G., and van Vliet, A. H. M. (2006) NikR Mediates Nickel-Responsive Transcriptional Repression of the *Helicobacter pylori* Outer Membrane Proteins FecA3 (HP1400) and FrpB4 (HP1512), *Infect. Immun. 74*, 6821−6828.
14. Delany, I., Ieva, R., Soragni, A., Hilleringmann, M., Rappuoli, R., and Scarlato, V. (2005) In Vitro Analysis of Protein-Operator Interactions of the NikR and Fur Metal-Responsive Regulators of Coregulated Genes in *Helicobacter pylori*, *J. Bacteriol. 187*, 7703−7715.
15. Pennella, M. A., Shokes, J. E., Cosper, N. J., Scott, R. A., and Giedroc, D. P. (2003) Structural elements of metal selectivity in metal sensor proteins, *Proc. Natl. Acad. Sci. U.S.A. 100*, 3713−3718.
16. Wang, S. C., Dias, A. V., Bloom, S. L., and Zamble, D. B. (2004) Selectivity of Metal Binding and Metal-Induced Stability of *Escherichia coli* NikR, *Biochemistry 43*, 10018−10028.
17. Dias, A. V., and Zamble, D. B. (2005) Protease digestion analysis of *Escherichia coli* NikR: Evidence for conformational stabilization with Ni(II), *J. Biol. Inorg. Chem. 10*, 605−612.
18. Leitch, S., Bradley, M. J., Rowe, J. L., Chivers, P. T., and Maroney, M. J. (2007) Nickel-Specific Response in the Transcriptional Regulator, *Escherichia coli* NikR, *J. Am. Chem. Soc. 129*, 5085−5095.
19. Schreiter, E. R., Sintchak, M. D., Guo, Y., Chivers, P. T., Sauer, R. T., and Drennan, C. L. (2003) Crystal structure of nickel-responsive transcription factor NikR, *Nat. Struct. Biol. 10*, 794−799.
20. Schreiter, E. R., Wang, S. C., Zamble, D. B., and Drennan, C. L. (2006) NikR-operator complex structure and the mechanism of repressor activation by metal ions, *Proc. Natl. Acad. Sci. U.S.A. 103*, 13676−13681.
21. Dian, C., Schauer, K., Kapp, U., McSweeney, S. M., Labigne, A., and Terradot, L. (2006) Structural Basis of the Nickel Response in *Helicobacter pylori*: Crystal Structures of HpNikR in Apo and Nickel-bound States, *J. Mol. Biol. 361*, 715−730.
22. Chivers, P. T., and Tahirov, T. H. (2005) Structure of *Pyrococcus horikoshii* NikR: Nickel Sensing and Implications for the Regulation of DNA Recognition, *J. Mol. Biol. 348*, 597−607.
23. Otwinowski, Z., and Minor, W. (1997) Processing of X-ray Diffraction Data Collected in Oscillation Mode, *Methods Enzymol. 276*, 307−326.
24. Kissinger, C. R., Gehlhaar, D. K., and Fogel, D. B. (1999) Rapid automated molecular replacement by evolutionary search, *Acta Crystallogr. D55*, 484−491.
25. Brünger, A. T., Adams, P. D., Clore, G. M., DeLano, W. L., Gros, P., Grosse-Kunstleve, R. W., Jiang, J. S., Kuszewski, J., Nilges, M., Pannu, N. S., Read, R. J., Rice, L. M., Simonson, T., and Warren, G. L. (1998) Crystallography & NMR system: A new software suite for macromolecular structure determination, *Acta Crystallogr. D54*, 905−921.
26. McRee, D. E. (1999) XtalView/Xfit: A Versatile Program for Manipulating Atomic Coordinates and Electron Density, *J. Struct. Biol. 125*, 156−165.
27. Emsley, P., and Crowtan, K. (2004) Coot: Model-building tools for molecular graphics, *Acta Crystallogr. D60*, 2126−2132.
28. Collaborative Computational Project, Number 4 (1994) The CCP4 Suite: Programs for Protein Crystallography, *Acta Crystallogr. D50*, 760−763.
29. Leslie, A. G. W. (1992) Recent changes to the MOSFLM package for processing film and image plate data, *Joint CCP4 and ESF-EAMCB Newsletter on Protein Crystallography*, No. 26.
30. Collaborative Computational Project No. 4 (1994) The CCP4 Suite: Programs for Protein Crystallography, *Acta Crystallogr. D50*, 760−763.
31. Storoni, L. C., McCoy, A. J., and Read, R. J. (2004) Likelihood-enhanced fast rotation functions, *Acta Crystallogr. D60*, 432−438.
32. Atanassova, A., Lam, R., and Zamble, D. B. (2004) A high-performance liquid chromatography method for determining transition metal content in proteins, *Anal. Biochem. 335*, 103−111.
33. Gill, S. C., and von Hippel, P. H. (1989) Calculation of protein extinction coefficients from amino acid sequence data, *Anal. Biochem. 182*, 319−326.
34. Greenfield, N. J., and Fasman, G. D. (1969) Computed circular dichroism spectra for the evaluation of protein conformation, *Biochemistry 8*, 4108−4116.
35. Morrisett, J. D., David, J. S. K., Pownall, H. J., and Gotto, A. M. (1973) Interaction of an apolipoprotein (apoLP-alanine) with phosphatidylcholine, *Biochemistry 12*, 1290−1299.
36. Taylor, J. W., and Kaiser, E. T. (1987) Structure-function analysis of proteins through the design, synthesis, and study of peptide models, *Methods Enzymol. 154*, 473−498.
37. Kleywegt, G. J., and Jones, T. A. (1994) A super position, *Joint CCP4 and ESF-EACBM Newsletter on Protein Crystallography 31*, 9−14.
38. Rulisek, L., and Vondrasek, J. (1998) Coordination geometries of selected transition metal ions (Co^{2+}, Ni^{2+}, Cu^{2+}, Zn^{2+}, Cd^{2+}, and Hg^{2+}) in metalloproteins, *J. Inorg. Biochem. 71*, 115−127.
39. Finney, L. A., and O'Halloran, T. V. (2003) Transition metal speciation in the cell: Insights from the chemistry of metal ion receptors, *Science 300*, 931−936.
40. Rosenzweig, A. C. (2001) Copper delivery by metallochaperone proteins, *Acc. Chem. Res. 34*, 119−128.

BI702006H